https://doi.org/10.5194/egusphere-2026-4816
Preprint. Discussion started: 5 November 2026
© Author(s) 2026. CC BY 4.0 License.

Multi-frequency seismo-acoustic measurements of synthetic ice with fluid inclusions: implications for seismic and through-ice acoustic estimation of sea-ice thickness

Sourav Sahoo[1], Laurence North[1], Madhu B.N. Murthy[2], Gaye Bayrakci[1] and Angus I. Best[1]

[1]National Oceanography Centre, Southampton, UK
[2]University of Southampton, Southampton, UK

Correspondence to: Sourav Sahoo (s.sahoo@noc.ac.uk)

Abstract

We conducted laboratory measurements of synthetic ice cores designed to mimic natural ice with variable fluid-inclusion content, primarily air inclusions and possible unfrozen water, using two frequency bands: P-wave velocity and attenuation at 4–10 kHz using an acoustic pulse tube, and P- and S-wave velocities and attenuation at ~300 Hz using a resonant column. Four synthetic ice cores of ~69 mm diameter were produced by directional freezing from above with water circulation using reverse osmosis water, providing control over inclusion concentrations. We classified the cores based on densities above and below 900 kg m^{-3}. Two higher-density cores (>900 kg m^{-3}) showed P-wave velocities of 3100 to 3500 m s^{-1} at 4 to 10 kHz and ~3400 m s^{-1} at ~300 Hz, with P-wave attenuation expressed as the inverse quality factor Qp^{-1} generally below 0.1. Two lower-density cores (852 to 886 kg m^{-3}) showed lower P-wave velocities of 2500 to 2800 m s^{-1} at 4 to 10 kHz and approximately 3100 m s^{-1} at ~300 Hz, with more variable attenuation and Qp^{-1} values reaching up to ~0.2. S-wave velocities at ~300 Hz were approximately 1250 m s^{-1} for the higher-density core and 1050 to 1150 m s^{-1} for the lower-density core, with Qs^{-1} ranging from 0.13 to 0.25 and from 0.23 to 0.31, respectively. These results indicate that lower bulk density, used here as a proxy for higher air inclusion concentration, is associated with reduced P and S-wave velocities and generally higher attenuation. The S-wave properties of the lower-density core were sensitive to applied strain during torsional vibration, with decreasing shear-wave velocity and increasing attenuation at higher applied strains. This suggests that lower-density ice cores has a more compliant and dissipative microstructure than higher-density ice cores. We adapted an effective medium sediment model originally developed for hydrate bearing sediment to ice, enabling joint interpretation of the pulse tube and resonant column data. The model captures the main trends in velocity and attenuation across both frequency bands and shows that permeability and gas bubble size strongly influence the elastic-wave properties. This dataset provides a reference for interpreting seismic and through-ice acoustic measurements of sea-ice thickness, in which part or all of the measured wavefield propagates within the ice. Our results suggest that air inclusions and possible unfrozen water can cause velocity variations of approximately 20–25% in our measured frequency range of ~300 Hz and 4–10 kHz. If unaccounted for, these variations may lead to substantial errors in sea ice thickness estimates from geophysical velocity measurements derived from seismic or through-ice acoustic travel times. For example, for a 1 m thick ice layer, interpreting the same travel time using the measured end-member acoustic velocities would give apparent thicknesses of approximately 0.80–1.25 m, corresponding to potential errors of about 0.20–0.25 m.

https://doi.org/10.5194/egusphere-2026-4816
Preprint. Discussion started: 5 November 2026
© Author(s) 2026. CC BY 4.0 License.



Keywords

Synthetic ice formation, Fluid inclusions, Acoustic pulse tube, Resonant column, P- and S-wave velocity and attenuation, Strain and frequency dependence

https://doi.org/10.5194/egusphere-2026-4816
Preprint. Discussion started: 5 November 2026
© Author(s) 2026. CC BY 4.0 License.

1. Introduction

Sea ice is a key component of the cryosphere, affecting climate, hydrology, and polar operations. The rapid decline in Arctic sea ice extent and thickness over recent decades has created a need for improved monitoring capabilities(Bocquet et al., 2024; Sumata et al., 2023). Geophysical methods using acoustic and seismic techniques offer a way to characterize ice from various platforms including ships, ice-based stations, airborne systems, and autonomous underwater vehicles (Figure 1 of Hills et al., 2025; Sun et al., 2003). Reliable interpretation of acoustic and seismic measurements requires robust knowledge of elastic wave properties in ice and how these properties depend on internal structure .(e.g., Bassett et al., 2020; Chotiros et al., 2023).

Sea ice structure may even be affected by relative motion of ice sheets, collisions and the build-up of pressure ridges. As such, sea ice of various thicknesses (from a few centimetres to several metres) can exhibit a range of mechanical properties (e.g. strength, brittleness, load-bearing capacity) and a range of acoustic properties. It is well known that imperfections such as inclusions and fractures in an otherwise homogenous medium can affect acoustic properties (e.g., Mavko et al., 2009), and hence there is potential for remote acoustic measurements to provide information on intrinsic sea ice properties.

Field measurements of ice thickness using acoustics have been applied in both marine and terrestrial cryospheric settings. In the sea-ice context, upward-looking sonar systems have long been used to measure ice draft, with total thickness inferred indirectly through hydrostatic assumptions and estimates of ice and snow density (e.g., Garrison, Knapp, et al., 1991). More recently, Bassett et al. (2020) demonstrated that broadband acoustic backscattering measurements can resolve reflections from both the ice–water and ice–air interfaces, enabling direct estimation of first-year sea-ice thickness under favourable conditions, with validation against ice-core measurements. Numerical and field-based studies further show that the acoustic response of sea ice depends on multiple coupled parameters, including thickness, elastic properties, attenuation, and roughness, which complicates interpretation of sonar returns in natural settings (Chotiros et al., 2023; Xu et al., 2025).

Analogous approaches have been widely applied in glacial environments, where active and passive seismic methods are routinely used to estimate ice thickness and basal geometry. Traditional seismic reflection and refraction surveys have been used to determine glacier thickness and bed properties across a range of alpine and polar settings, often in combination with radar or borehole observations (e.g., Podolskiy & Walter, 2016). More recently, distributed acoustic sensing (DAS) techniques have enabled high-resolution acoustic and seismic measurements on glacier surfaces and within boreholes, allowing glacier thickness and internal structure to be inferred directly from wave travel times and dispersion characteristics (Booth et al., 2020; Walter et al., 2020). Field experiments using DAS and active seismic sources have shown that ice thickness can be recovered from guided-wave dispersion and reflected phases, with results consistent with independent thickness measurements (Agnew et al., 2026; Nziengui-Bâ et al., 2023). These studies demonstrate that acoustic and seismic wave propagation in ice contains sufficient information to constrain ice thickness, provided that the frequency band and the influence of internal heterogeneity are appropriately accounted for.

Long-duration acoustic monitoring from below sea-ice has also demonstrated the value of upward-looking sonar for characterizing sea-ice draft and underside morphology. Hudson (1990) used an upward-looking sonar to obtain long-duration measurements of sea-ice draft and keel properties in the Canadian Beaufort Sea, while Melling and Riedel (1995) used subsea sonars to characterize underside topography and draft distributions over the Beaufort Sea continental shelf. These studies primarily constrain ice draft rather than total thickness, but they demonstrate the long-standing potential of acoustic monitoring from below for quantifying sea-ice morphology over extended temporal and spatial scales.

More recently, broadband acoustic approaches have explored the possibility of estimating full ice thickness using higher-frequency systems. Bassett et al. (Bassett et al., 2015) reported laboratory measurements of acoustic backscatter from sea ice in the 200–565 kHz range, which was later extended to 75–590 kHz(Bassett et al., 2016). Subsequent work demonstrated that thickness can be inferred from the time delay between water–ice and ice–air echoes using broadband measurements in the 75–130 kHz band(Bassett et al., 2018), while Bassett et al. (2020) further examined this range and predicted useful operation over approximately 45–155 kHz. These studies employ an upward-looking acoustic configuration, with sensors located beneath the ice, but remain within a high-frequency broadband regime.

https://doi.org/10.5194/egusphere-2026-4816
Preprint. Discussion started: 5 November 2026
© Author(s) 2026. CC BY 4.0 License.

Lower acoustic frequencies may offer additional advantages for such applications. Acoustic attenuation in sea ice increases strongly with frequency, rising from about 0.45 dB m^{-1} at 10 kHz to about 4.5 dB m^{-1} at 100 kHz and more than 35 dB m^{-1} at 500 kHz (Langleben, 1969), suggesting that lower-frequency signals may penetrate more effectively through the ice. Longer wavelengths may also reduce sensitivity to small-scale ice structure, improving robustness in heterogeneous or strongly scattering ice. The practical relevance of this regime is reflected in under-ice field studies, such as the 4–8 kHz transmission and communication experiments reported by Tollefsen et al. (2023).

Natural ice exhibits complex internal structures that result from formation processes, temperature gradients, and dynamics. Ice can contain air bubbles, unfrozen water pockets, and different crystal arrangements. These heterogeneities, particularly fluid inclusions, strongly influence elastic wave propagation, affecting both P-wave and S-wave velocities and attenuations. While acoustic properties of solid, bubble-free ice are relatively well constrained (e.g., Vogt et al., 2008), the effects of gas and liquid inclusions and microstructure on frequency-dependent wave propagation remain less well constrained.

The influence of ice properties on thickness estimation depends on the measurement configuration. Conventional upward-looking sonar measures the travel time through seawater to the ice–water interface and therefore primarily determines ice draft, with total thickness subsequently estimated using hydrostatic assumptions. By contrast, seismic reflection, refraction, guided-wave and through-ice acoustic methods include propagation within the ice. In these configurations, the assumed P- or S-wave velocity directly affects the conversion of measured travel times or dispersion characteristics into ice thickness. The laboratory measurements presented here are intended primarily to constrain these velocity-dependent seismic and through-ice acoustic applications. The results are therefore intended for researchers interpreting active-seismic, distributed acoustic sensing, guided-wave, cross-hole and through-ice acoustic observations of sea ice, lake ice and glacier ice.

Additional challenges arise due to preservation of natural ice samples, such as maintaining *in situ* pressure and temperature conditions. Hence, laboratory formation of synthetic ice can provide a better control of internal structural variations, needed to inform our understanding and theoretical modelling of acoustic properties. We need this fundamental understanding of frequency dependent acoustic properties and theoretical modelling, to inform the interpretation of ice thickness and mechanical properties from remote sensing.

The few published laboratory acoustic measurements of sea ice are of homogeneous, unfractured and bubble-free sea ice (e.g., Garrison, Francois, et al., 1991; Light et al., 2003). The measurement methods used in such previous studies added some additional uncertainties; for example, low frequency (100 Hz – 10 kHz) measurements of P-wave velocity were performed indirectly by measuring torsional flexure waves in ice bar samples. The resulting torsional stiffness was then used to derive the shear (S-wave) elastic modulus, then the bulk modulus (using an assumed value of Poisson's ratio), and hence P-wave (body wave) velocity. The measurement and data manipulation stages, together with large uncertainty in Poisson's ratio, contribute to large intrinsic errors associated with this indirect measurement method (Garrison, Francois, et al., 1991).

Here, we focused on producing synthetic ice samples representative of selected heterogeneous features of natural sea ice. We achieved this by closely imitating natural sea ice formation processes, namely the freezing of surface water from cooled air above, with fluid circulation at the base of the water column during ice formation. The objective is to quantify how fluid inclusions affect the elastic properties required to interpret seismic and through-ice acoustic measurements of ice thickness. We measured P- and S-wave velocity and attenuation at frequencies relevant to seismic and low-frequency acoustic applications and used effective-medium modelling to investigate the sensitivity of these properties to inclusion-related parameters. The freshwater samples isolate the effects of air and possible unfrozen-water inclusions but do not reproduce the saline brine network of natural sea ice.

2. Materials and Methods

2.1 Synthetic ice core preparation

https://doi.org/10.5194/egusphere-2026-4816
Preprint. Discussion started: 5 November 2026
© Author(s) 2026. CC BY 4.0 License.

We devised a bespoke ice making apparatus to mimic natural sea ice formation that includes circulating water with freezing from above (Figure 1). When ice forms, the dissolved gas (air) in the liquid (water) comes out of solution and becomes trapped as gas inclusions in the ice as the water freezes. By controlling the fluid circulation speed, we were able to create heterogeneous ice samples with different amounts and sizes of fluid inclusions. This method is modified from previous studies using similar techniques, but on a different scale (e.g., Johnson et al., 2021; Weissenberger & Grossmann, 1998). Whereas earlier studies produced metre-scale ice in large tanks to examine processes such as seeding, supercooling, biological incorporation, circulation, and wave action, our apparatus was designed to produce cylindrical cores that imitate field-recovered ice cores and are suitable for acoustic pulse tube and resonant column measurements.

We were able to create several synthetic ice specimens or "cores" (69 mm diameter cylindrical cores, 250 – 350 mm long), with varying bulk density and inclusion content. We measured bulk density directly for each core and use it here as the primary basis for comparison. For clarity, cores with densities >900 kg m^{-3} are referred to throughout as higher-density cores, whereas those with densities <900 kg m^{-3} are referred to as lower-density cores. We measured P-wave velocity and attenuation in the acoustic frequency range (4 – 10 kHz) using NOC's Acoustic Pulse Tube facility (Sutiyoso et al., 2024), and P- and S-wave velocity and attenuation at lower frequencies (~300 Hz) using the University of Southampton's geotechnical resonant column (Priest et al., 2005).

Our elastic wave measurement systems are configured for cylindrical geological core samples of 7 cm diameter, with sample lengths up to 50 cm in the pulse tube, and up to 14 cm in the resonant column. Hence, we used a steel tube of internal diameter 7 cm filled with Reverse Osmosis (RO) water, insulated on the sides with the top left open to the surrounding air inside the freezer at -24 °C, thus allowed freezing from the top. Water was circulated in the steel tube while freezing, similar to sea-water circulation under natural sea ice formation conditions.

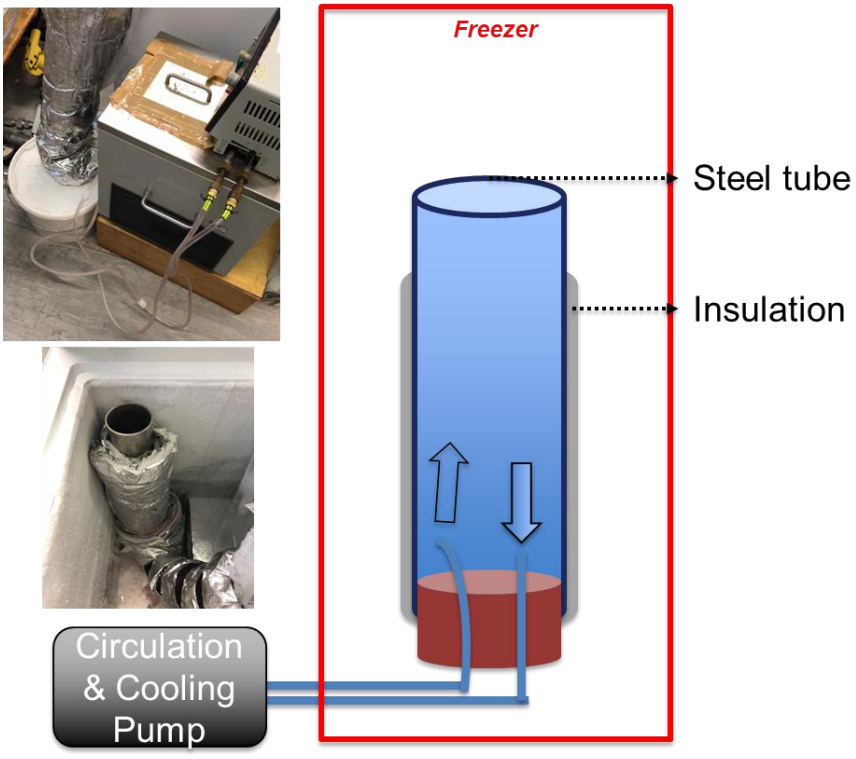


Figure 1: Method to form ice cores which allows freezing from the top open to the air, and water circulation at the enclosed base of a steel tube (internal diameter 69 mm), all held within a freezer at a temperature of -24 °C.

https://doi.org/10.5194/egusphere-2026-4816
Preprint. Discussion started: 5 November 2026
© Author(s) 2026. CC BY 4.0 License.

The circulation fluid pipes were also insulated to prevent them from freezing. The setup was left in this condition to allow ice formation, taking almost one month to form one core. Once the ice had formed, sample was removed from the freezer and then insulation was removed. The insulation was removed slowly to ensure no sudden temperature change occurred, which could have fractured the sample. The steel tube was kept at room temperature for 2 hours so that the outer edge of the ice core melted slightly, allowing the core to be removed while minimising mechanical damage.

The ice core was then kept in the freezer until it was time for the acoustic measurements. Both ends of the core were made flat before acoustic measurements in the pulse tube, as planar end interfaces at right angles to the side walls are required; this was achieved using a saw and warm plate (at 30 ºC).

The method described above allows for changes in circulation water speed and temperature control. In principle, different volumes of fluid inclusions can be achieved by controlling the circulation speed, freezer and circulating fluid temperatures. We did several tests to find the optimum conditions for forming solid ice. When the circulation speed is too high, we found that the water does not freeze even after two months. When the circulation speed is too low, water freezes with more trapped gas. We selected a subset of cores based on visual similarity to published images of natural sea ice samples for pulse tube and resonant column measurements. For example, during our experiment we found some ice broke off when removed from the steel tube, while some cores had not fully formed when we removed them from the steel tube. We used RO water to avoid complications of corrosion of equipment. Glacial ice provides the most appropriate natural analogue for interpreting the resulting microstructure, because both materials form from freshwater and contain air as the dominant inclusion phase. In glacial ice, air was trapped during densification from firn, an intermediate material formed by the compaction of snow before it becomes glacier ice. This trapped air persists as bubbles whose size, shape, and connectivity evolve with pressure and deformation, producing a heterogeneous polycrystalline material with strong elastic contrasts between the ice matrix and fluid inclusions (Bader, 1950; Sammonds et al., 2017).

2.2 Acoustic pulse tube experiments

The acoustic pulse tube used for measuring P-wave velocity and attenuation at sonic frequencies is shown in Figure 2. The stainless-steel pressure tube was filled with reverse osmosis water, and the ice core was floated at the top of the water column with its upper surface exposed to air, thereby imitating the acoustic boundary condition of floating ice. The acoustic source is located at the base of the tube, and two hydrophones mounted in the tube wall record the acoustic response below the ice core.

The pulse tube measures the acoustic response of a sample to a swept-frequency acoustic stimulus between 4 and 10 kHz. The acoustic pulse tube is treated here as a water-filled, thick-walled stainless-steel acoustic waveguide. When the wall of an acoustic waveguide, such as a fluid filled pulse tube, has finite shear modulus, a Stoneley wave propagates in the fluid with velocity smaller than the P-wave. The Stoneley wave dispersion is small when the density of the fluid is a small fraction of the density of the sidewall material. In an ideal fluid-filled tube with infinitely rigid walls, there would be no elastic coupling between the fluid and the tube wall, and the acoustic field could be treated as a plane wave below the cut-off frequency for higher-order modes. In practice, no material is infinitely rigid, and real water-filled tubes can support weak elastic waveguide effects caused by coupling between the fluid and the tube wall, including dispersion, radial particle motion and wavefront curvature. Del Grosso (1971) developed the elastic waveguide formulation for liquid-filled cylindrical tubes with elastic walls, and Wilson et al. (2003) used this formulation to evaluate stainless-steel tube dimensions. They showed that a wall-thickness to inner-radius ratio close to unity gives less than 1% dispersion in the lowest-order mode up to approximately the rigid-wall waveguide cut-off frequency. The NOC pulse tube used here has an internal diameter of 70 mm, an inner radius of 35 mm and a wall thickness of 182 mm, giving a wall-thickness to inner-radius ratio of 5.2, much greater than that needed for < 1% dispersion. The tube therefore provides a very stiff, thick-walled approximation to a rigid acoustic waveguide. Additional COMSOL finite-element modelling of the pulse-tube geometry indicated that acoustic transmission through the stainless-steel wall is negligible over the measurement frequency band, supporting the assumption that the measured response is dominated by guided propagation within the water-filled tube and ice core.

https://doi.org/10.5194/egusphere-2026-4816
Preprint. Discussion started: 5 November 2026
© Author(s) 2026. CC BY 4.0 License.

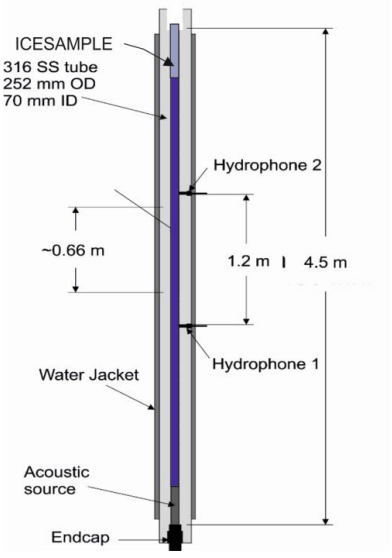


Figure 2: Ice core measurements in the NOC acoustic pulse tube. The stainless-steel pressure tube is filled with reverse osmosis water and the ice core floats on top, open to air. The acoustic source is at the bottom of the tube, and two hydrophones are placed in the middle, as shown in the figure.

We used the spectral ratio of signal amplitudes of reflections from the ice/water interface obtained from Hydrophones 1 and 2 in Figure 2. We obtained acoustic velocity and attenuation spectra of a core using a non-linear inversion method (Appendix A), giving a spectral resolution of 833 Hz. We generated an idealised one-dimensional forward model of the ice core and water-filled pulse tube. This 1D model does not account for any reflections from the side wall of pulse tube. Then we employed a derivative-free optimisation algorithm to deduce a best fit velocity and attenuation for the sample by fitting measured and forward model data (Appendix A). The output of this process is a complex velocity; The P-wave attenuation (Q_p^{-1}, where Q_p is P-wave quality factor) is given by the ratio of the imaginary to real part of the complex velocity, while the P- velocity (V_p) is the real part (Mavko et al., 2009). The details of the pulse tube velocity and attenuation calculation are given in Appendix A. The pulse tube design is based on concepts described in McCann et al. (2014), with significant enhancements to enable frequency dependent measurements of P-wave velocity and attenuation. The pulse tube data acquisition and calibration is discussed in detail by Sutiyoso et al. (2024) and it has already provided reliable measurements for sand and ice bearing samples (Sutiyoso et al., 2024, 2025, 2026).

In general, the inverse quality factor Q^{-1} is related to the velocity V and attenuation coefficient α by

$$\frac{1}{Q} = \frac{V.\alpha}{\pi.f}, \quad (1)$$

where f is signal frequency and α has units of Nepers/metre [1 Neper/m = 8.686 dB/m].

Note that the attenuation in the water below the ice core is included in our calculation of ice attenuation in this case. As attenuation in water is very small (4.3×10^{-5} dB/m at 3.5 °C; Ainslie and McColm, 1998) compared to that of ice (order of 1 – 10 dB/m), this does not affect the results. It was made sure that no air was trapped below the ice by tilting the ice and allowing any trapped air to be released. The presence of air below the ice core strongly attenuates the acoustic waves due to the nearly -1 reflection coefficient of water to air, leading to unrepresentative measurements and errors and such measurements were checked to make sure no air is trapped. A temperature of 3.5 °C was maintained in the pulse tube during the experiments.

We calibrated the pulse tube measurements using a standard nylon sample (Figure 3) and saturated sand sample of known properties (Sutiyoso et al., 2024). Nylon has density of 1120 $kg.m^{-3}$ although its acoustic velocity of

https://doi.org/10.5194/egusphere-2026-4816
Preprint. Discussion started: 5 November 2026
© Author(s) 2026. CC BY 4.0 License.

2600 m/s (at 5 MHz) is lower than expected for ice (3000 - 3500 m/s), and attenuation coefficient α of around 0.3 dB/m at 5 kHz. Selfridge (1985) gives a value of 290 dB/m at 5 MHz and then we can infer a value at 5 kHz using

$$\alpha = k.\, f, \qquad (2)$$

where f is frequency and k is a constant calculated from the given figures). Using Equation 1, with V=2600 m s^{-1} and α=0.0345 Np m^{-1}, this is equivalent to Q^{-1}≈0.006.The Nylon sample diameter was 6.8 cm with length 48 cm, ensuring the nylon sample is not mechanically coupled to the pulse tube wall. While ice floats in water, the nylon sample is denser than water and hence was held in place using a thin thread made from nylon 66.

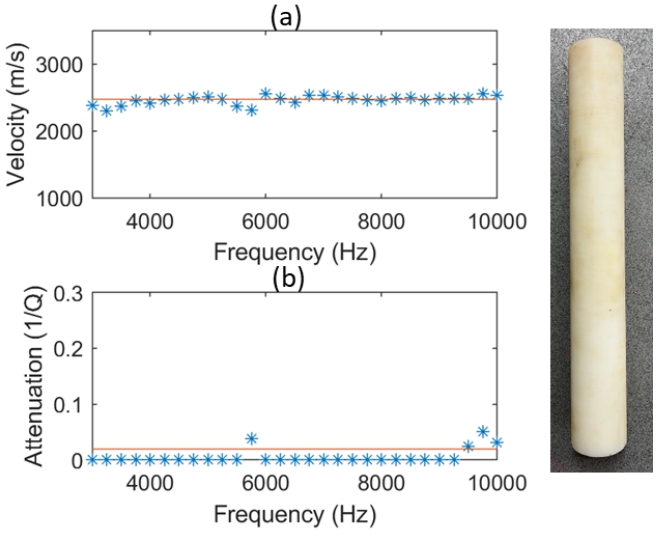


Figure 3: Measurement of acoustic velocity and attenuation of a 23.5 cm long nylon sample for calibration. Pulse tube data is shown as blue stars; the red line shows the constant velocity estimate. The attenuation is too low to be measured accurately and hence the inversion shows it as zero.

The nylon results in Figure 3 show a P- wave velocity around 2500 m/s ± 10 % that remains almost constant across the frequency range from 4 – 10 kHz; the spectral variations are an indication of the acoustical imperfections in the pulse tube versus the idealised inversion model (e.g. side wall transducer ports give extra reflections, etc.). The zero attenuation results from the inversion procedure indicate the attenuation is too small to be resolved in this case, consistent with the small value for Nylon inferred above.

2.3 Resonant Column

The Gas Hydrate Resonant Column (GHRC) was originally developed for measuring the low frequency (<500 Hz) geophysical properties of hydrate-bearing sediments for marine geophysical studies (Clayton et al., 2005). However, it also lends itself to ice sample measurements because of its rigidity and cold temperature control ability compared to standard geotechnical resonant column apparatus on which its design is based. It enables accurate measurements of P- and S-wave velocity and attenuation of cylindrical samples 7 cm in diameter, 14 cm long under elevated pressure (up to 20 MPa) and temperatures between -18 to 22 °C (Clayton et al., 2005). It measures the forced vibration natural resonance frequency of samples that generally fall below 500 Hz and depends on the resonant mode and sample elastic properties; the free vibration resonance amplitude decay curve is also measured. From these measurements and sample density, the velocity and attenuation of different vibration modes (torsional, extensional, longitudinal flexure) and their associated elastic properties (shear modulus, compressional modulus, Young's modulus and Poisson's ratio) can be derived. Of particular interest here are the S-wave velocity and derived dynamic shear wave modulus, needed for inferring material strength properties.

https://doi.org/10.5194/egusphere-2026-4816
Preprint. Discussion started: 5 November 2026
© Author(s) 2026. CC BY 4.0 License.

The principle of resonant column testing is that the specimen is fixed at its base and excited at the top over a range of frequencies to identify the first-mode resonant frequency. During preliminary testing, one of the main challenges was obtaining a clear single resonance peak; in some tests, multiple closely spaced peaks were observed over a narrow frequency interval. Similar issues have been reported in the resonant-column literature and are commonly associated with specimen fixity, apparatus compliance, and interaction between the specimen and drive system (Clayton et al., 2009; Kumar & Clayton, 2007). To improve specimen fixity, water was injected through the bottom pedestal to form a thin water film over the porous disk. The apparatus was then cooled to 5^0C; thereafter, the ice specimen was mounted, and the temperature was reduced to the target test temperature so that the base of the ice specimen froze onto the pedestal. This procedure produced a more stable boundary condition and improved the clarity of the resonant response.

3. Results

3.1 Acoustic pulse tube

We present acoustic pulse tube results from two ice cores, ice core 1 and 2. Figure 4 shows the pulse tube results for ice core 1 which was 23.5 cm long, 6.7 cm in diameter with mass 748.5 g giving a density of 903 kg.m^{-3}. We observed a velocity V_p of 3100 - 3500 m/s and attenuation Q_p^{-1} of 0.05 to 0.10, over the reliable frequency range of approximately 5–9 kHz. Data near the edges of the 4–10 kHz sweep were excluded from interpretation because they are more susceptible to boundary and sample-size. The measured values are within the expected range for sea ice and bubble free ice of 3000 – 3500 m/s reported in the literature (e.g., Rajan et al., 2017; Vogt et al., 2008). Over the reliable central frequency range of approximately 5–9 kHz, the spectra are summarised using mean values for first-order comparison between cores, field-scale assessments, and previous studies. This does not imply that velocity or attenuation are frequency independent; attenuation in particular is expected to be frequency dependent and generally to increase with frequency. For ice core 1, the mean V_p is 3090 m/s with a standard deviation of 273 m/s (± 8.8%); similarly, the mean value of attenuation is 0.06 ± 0.04.

https://doi.org/10.5194/egusphere-2026-4816
Preprint. Discussion started: 5 November 2026
© Author(s) 2026. CC BY 4.0 License.

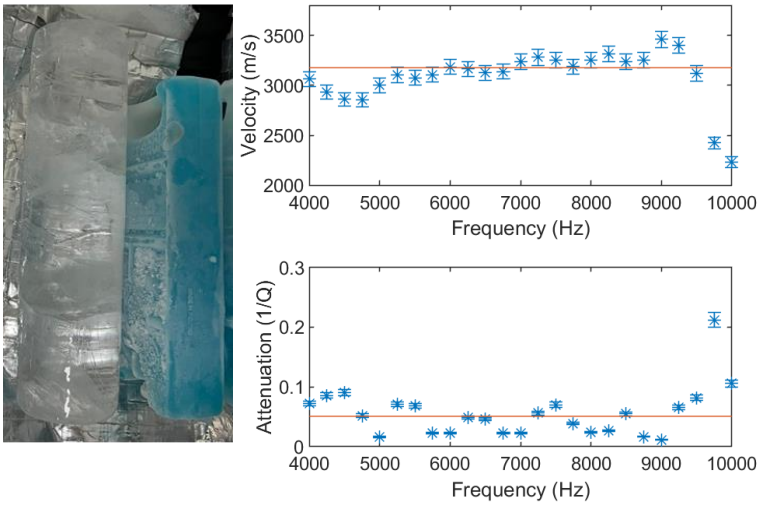


Figure 4: Measurement of acoustic velocity and attenuation of ice core 1, measuring 23.5 cm long, 6.7 cm in diameter and a density of 903 kg.m^{-3}. Pulse tube data are shown as blue stars; red lines show the mean constant velocity and attenuation of the blue starts across frequency.

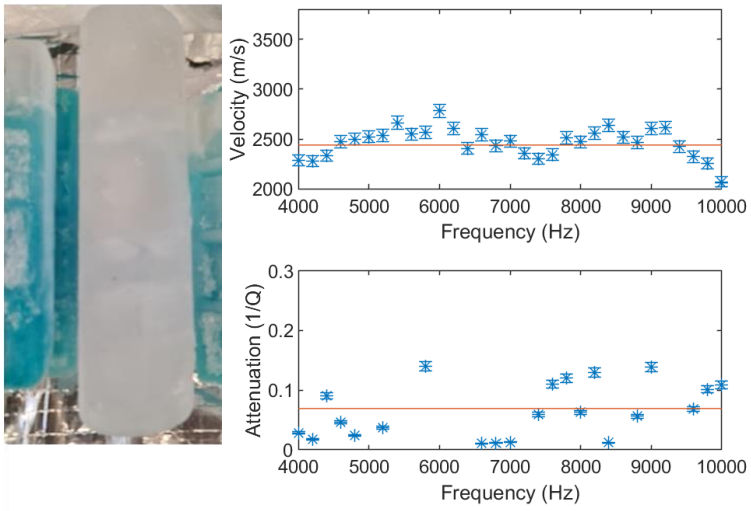


Figure 5: Measurement of velocity and attenuation of 23.6 cm long lower-density ice core 2 (851.8 kg m^{-3}). Pulse tube data are shown as blue stars; red lines show the mean constant velocity and attenuation.

The ice core 2, has a length of 23.6 cm and a diameter of 6.8 cm with mass 730.1 g giving a density of 851.8 kg.m^{-3} (Figure 5). Visual inspection shows that ice core 2 contains more visible air inclusions than ice core 1, consistent with its lower measured density and more heterogeneous inclusion distribution. Observed velocity ranged between 2500 - 2800 m/s (mean 2465 m/s with standard deviation of 146 m/s over the frequency range) and attenuation between 0 - 0.2 (mean 0.03 with standard deviation of 0.07), with gradual changes in velocity

https://doi.org/10.5194/egusphere-2026-4816
Preprint. Discussion started: 5 November 2026
© Author(s) 2026. CC BY 4.0 License.

over the frequency spectrum. The mean values provide a first-order comparison between cores, field-scale assessments, and previous studies. Velocity shows two broad convex features, with local maxima around approximately 5.5–6.0 kHz and 8.5–9.0 kHz, separated by a lower-velocity interval around 7–7.5 kHz. Attenuation is more variable with no apparent pattern.

In both cores, there is sharp decrease in velocity above 9 kHz. Both velocity and attenuation are lower in ice core 2 than for ice core 1 in Figure 4, broadly consistent with expected effects due to trapped air bubbles. For example, Anderson & Hampton (1980a) show that gassy water has much lower velocity below gas bubble resonance than gas-free water, and that attenuation is generally higher in gassy water.

3.2 Resonant Column Results

Resonant column tests were conducted in both torsional and flexural vibration modes on two other ice cores (ice core 3 and 4). We initially aimed to use the same sample to be measured in both systems, but this was not possible due to difficulties preserving cores between labs. The top and bottom plates of the apparatus were saturated with water to facilitate sample fixity, thereafter they were left undisturbed under constant temperature of –5 °C for 48 hours.

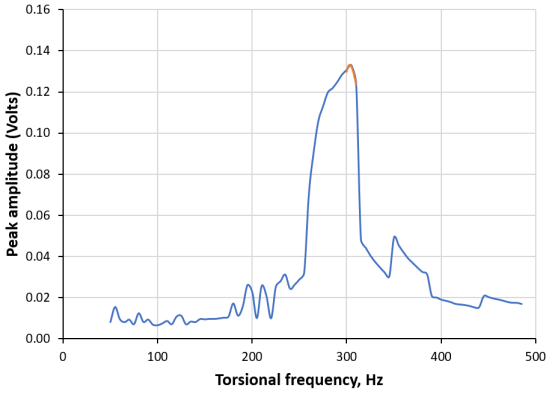


Figure 6: Amplitude of oscillation versus frequency under torsional excitation of ice core 3 (lower-density core; 886 kg m^{-3}).

Figure 6 shows a typical vibrational amplitude resonance response to the driving frequency between 50 – 450 Hz. Figure 7 shows the free vibrational amplitude response curves of ice core 3 from which attenuation is calculated (at the resonance frequency).

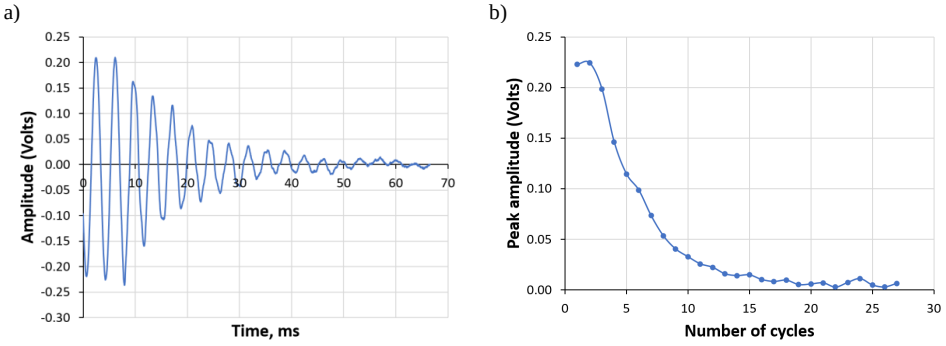


Figure 7: a) Free vibration amplitude response versus time from the torsional test on ice core 3. b) normalised peak amplitude versus number of cycles.

https://doi.org/10.5194/egusphere-2026-4816
Preprint. Discussion started: 5 November 2026
© Author(s) 2026. CC BY 4.0 License.

Figures 8a & 8b show the S-wave velocity (V_s) and S-wave attenuation (Q_s^{-1}) response to different applied shear strain (changing applied voltage) for ice core 3, respectively. V_s was found to be between 1150 to 1050 m/s at seismic strains (< 10^{-6}), showing a clear drop at higher strains that is typical of granular materials (Senetakis et al., 2016). Q_s^{-1} was obtained from the free vibration decay responses shown in Figure 7 with values between 0.23 to 0.31 at seismic strains (< 10^{-6}). There is a clear increase in Q_s^{-1} at higher shear strains, also typical of granular materials (Senetakis et al., 2016).

Figure 8c & 8d show P-wave velocity (V_p) and flexural wave attenuation (Q_f^{-1}) response to different applied flexural strains (changing applied voltage) for ice core 3 assuming a Poisson's ratio of 0.33. V_p was found to be 3100 m/s, and unlike for V_s, there is no drop with strain, which could be due to the assumed Poisson's ratio. Q_f^{-1} was obtained from the free vibration decay response (not shown) with values between 0.20 to 0.25 with no discernible trend.

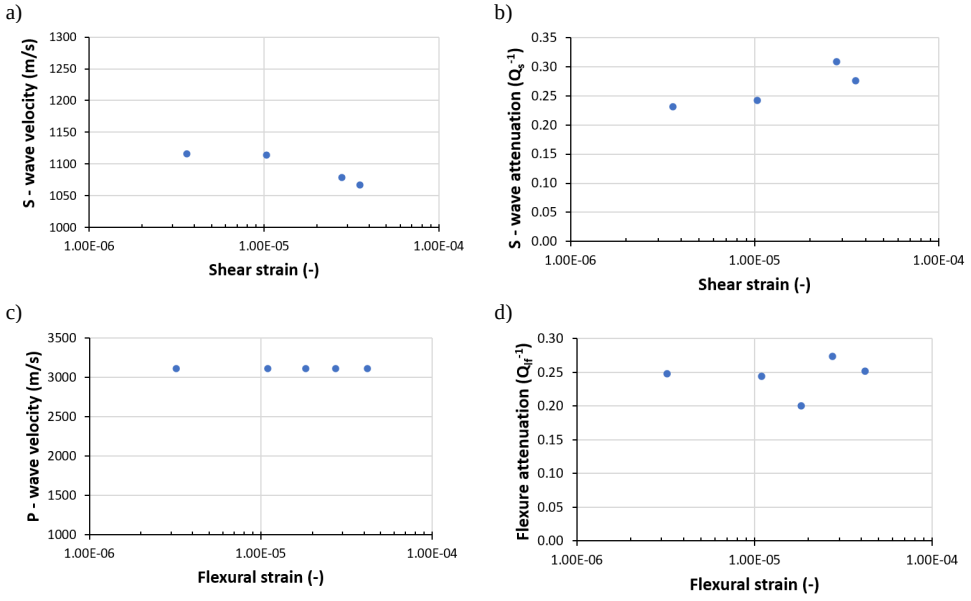


Figure 8: a) S-wave velocity, b) S-wave attenuation, c) P-wave velocity, and d) flexural wave attenuation versus applied strain from the torsional (a, b) and flexural (c, d) tests on ice core 13 (lower-density core; 886 kg m^{-3}).

V_p and Q_p^{-1} can be derived from the measured torsional and flexural values of V_s, V_{fl} and Q_{fl}^{-1} using an assumed or measured Poisson's ratio according to the mathematical relations (see Best et al., 2010)

$$V_p = V_{lf}\sqrt{\frac{1-\nu}{(1+\nu)(1-2\nu)}}, \quad (3)$$

where ν is Poisson's ratio given by

$$\nu = \frac{1}{2}\left(\frac{V_{lf}^2}{V_s^2}\right) - 1, \quad (3)$$

https://doi.org/10.5194/egusphere-2026-4816
Preprint. Discussion started: 5 November 2026
© Author(s) 2026. CC BY 4.0 License.

and

$$\frac{(1-\nu)(1-2\nu)}{Q_p} = \frac{(1+\nu)}{Q_{lf}} - \frac{2\nu(2-\nu)}{Q_s}. \quad (5)$$

Because the calculations of V_p and Q_p^{-1} each involve three measured parameters, with Poisson's ratio being particularly sensitive to measurement errors, the errors can multiply significantly. As reported in Best et al. (2010), calibration of the system using metal bars of standard materials gave accuracies of Vs ± 1%, V_{fl} ± 6%, and Q_s^{-1} and Q_{fl}^{-1} better than ± 20%.

Figures 9 show the strain-dependence results for ice core 4. Unlike ice core 3, no drop in V_p nor V_s were seen as applied strain increases, but Q_s^{-1} and Q_{lf}^{-1} decrease with strain above seismic strains. These effects are likely related to the fewer gas inclusions in ice core 4 compared to ice core 3. V_s was around 1250 m/s, whereas Q_s^{-1} ranged between 0.13 to 0.20. V_p was 3400 m/s and Q_f^{-1} ranged between 0.12 - 0.23.

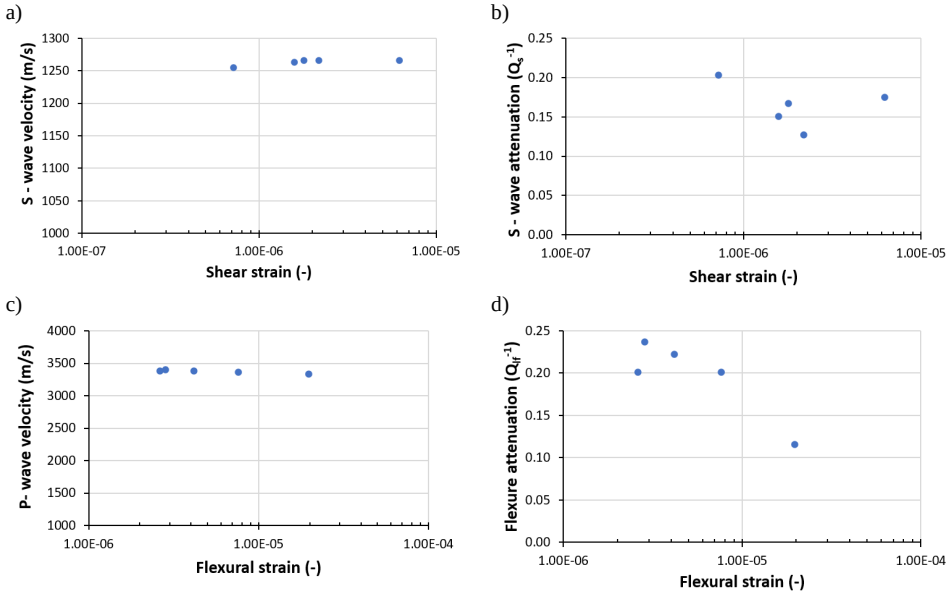


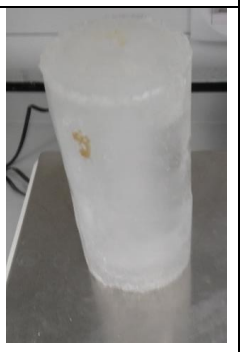
Figure 9: a) S-wave velocity, b) S-wave attenuation, c) P-wave velocity, and d) flexural wave attenuation versus strain from the torsional (a, b) and flexural (c, d) tests on ice core 4 (higher-density core; 905 kg m⁻³).

3.3 Comparison of acoustic pulse tube and resonant column results

The resonant column measurements at about 300 Hz show similar ranges of P-wave velocity and attenuation to the pulse tube measurements at 4 – 10 kHz for similar density cores (Table 1). The higher-density cores are ice core 1, measured using the pulse tube and presented in Column 1 of Table 1, and ice core 4, measured using the resonant column and presented in Column 4. The lower-density cores are ice core 2, measured using the pulse tube and presented in Column 2, and ice core 3, measured using the resonant column and presented in Column 3.

https://doi.org/10.5194/egusphere-2026-4816
Preprint. Discussion started: 5 November 2026
© Author(s) 2026. CC BY 4.0 License.

Table 1: Comparison of pulse tube and resonant column results.

Measured parameter	Acoustic pulse tube (4 – 10 kHz)		Resonant column (~ 300 Hz)	
	Ice core 1	Ice core 2	Ice core 3	Ice core 4
				
Density	903 kg.m^{-3}	851.8 kg.m^{-3}	886 kg.m^{-3}	905 kg.m^{-3}
Porosity (see section 3.4)	1.5%	7.1%	4.7%	1.45%
V_p (m/s)	3090 ± 273	2465 ± 146	3100 ± 120	3400 ± 180
V_s (m/s)	-	-	1150 - 1050	1220 - 1280
Q_p^{-1} {Q_{fl}^{-1}}	[0.06 ± 0.04] 0.061	[0.03 ± 0.07] 0.031	0.055 - 0.065 {0.20 to 0.25}	0.070 - 0.098 {0.12 - 0.23}
Q_s^{-1}	-	-	0.23 - 0.31	0.13 - 0.25

It is difficult to draw conclusions about velocity dispersion between lower frequency at c. 300 Hz and higher acoustic frequencies between 4 – 10 kHz. i.e. velocities should be higher at higher frequencies, consistent with poro-elastic models such as Biot's theory, because different cores were used in each frequency band. Here, we assume the flexural attenuation Q_{lf}^{-1} is broadly similar to P-wave attenuation Q_p^{-1}. In this context, dispersion refers to the dependence of wave velocity and attenuation on frequency.

These results are in line with previous measurements in glacial ice, for example sound speed of 3447±3 m/s was observed at frequencies between 2kHz to 35 kHz in Italian glacier ice Langenferner (Meyer et al., 2019).

3.4 Elastic wave propagation modelling

Elastic wave propagation modelling was used to provide a physical interpretation of the laboratory measurements and to explore which microstructural parameters could explain the observed velocity and attenuation variations between higher- and lower-density ice cores. In particular, the modelling allows us to test the sensitivity of the measured properties in both frequency ranges to inclusion-related parameters that were not directly measured, such as gas bubble size, permeability, and the relative proportions of air and unfrozen water in the pore space. This provides a first-order framework for assessing how inclusion-controlled heterogeneity may affect geophysical estimates of ice thickness.

We used the hydrate-bearing effective sediment model of Marín-Moreno et al. (2017) which combines Biot-type inertial fluid flow (Biot, 1956a, 1956b) and gas bubble resonance mechanisms. The model calculates frequency-dependent P-wave and S-wave velocities and attenuations from seismic (~ Hz) to ultrasonic frequencies (~MHz). Biot and subsequent authors (e.g., Mavko et al., 2009) formulated a wave propagation model for fluid saturated porous media that calculates frequency dependent P- and S-wave velocity and attenuation. It is a two-phase model

https://doi.org/10.5194/egusphere-2026-4816
Preprint. Discussion started: 5 November 2026
© Author(s) 2026. CC BY 4.0 License.

where one phase is the solid porous medium and the second phase is the pore fluid. It accounts for frequency-dependent inertial and viscous coupling between the two phases in relative motion when excited by a passing elastic wave, giving rise to elastic wave energy dissipation. This in turn leads to frequency-dependent velocity and attenuation of both P- and S-waves. Used extensively to describe successfully wave propagation in rocks, sediments and other porous media, here we adapted the model for porous ice and add the gas bubble resonance effects.

We assume the host medium is made of porous ice, with unfrozen water and air in the pore space. This abstraction is suitable for ice samples made from packs of ground ice particles with relatively high porosity, although we also apply it to our synthetic ice samples with fluid inclusions forming the main porosity.

We estimated porosity by measuring the bulk density of the ice cores. Initially, by assuming there is no unfrozen water, the difference in density between a solid ice core and the measured density is attributed to air inclusions, giving the porosity (i.e. ratio of the volume of air inclusions to the total core volume). Porosity can be calculated using the relation,

$$\rho = (1 - \varphi)\rho_s + \varphi.\rho_f \quad (6)$$

where ρ is sample bulk density, ρ_s is the solid ice density, ρ_f is the fluid density (air or water), and φ is porosity.

However, unfrozen water can indeed be present in ice and so we include hypothetical model results for different amounts of unfrozen water taking up part of the volume of the pore space of the ice; this is indicated by the pore space saturation of unfrozen water, S_u. This is the ratio of the volume of unfrozen water to the volume of pore space. Similarly, the remaining pore space is assumed to be occupied by air with a saturation, S_a.

$$S_u + S_a = 1.0. \quad (7)$$

Table 2: Values used in the Biot model for ice.

Parameter	Value	Units	Reference
Ice bulk modulus	8.6×10^9	Pa	(Leclaire et al., 1994)
Ice shear modulus	3.8×10^9	Pa	(Leclaire et al., 1994)
Ice density	917	Kg/m^3	(Hobbs, 2010)
Water density	1000	Kg/m^3	(Leclaire et al., 1994)
Water bulk modulus	2.25×10^9	Pa	(Leclaire et al., 1994)
Ice grain size	100×10^{-6}	m	
Critical porosity	0.85		

We applied our model to the results of both the pulse tube and the resonant column (Figure 10 and 11 respectively). Although these datasets correspond to different physical samples prepared using similar protocols, consistent trends emerge across the two frequency bands.

The model input parameters are shown in Table 2. The fixed parameters were chosen from measured sample properties where available, or from published values for ice and water. Parameters that were not measured directly, particularly permeability and gas bubble radius, were treated as sensitivity parameters rather than prescribed values. We first varied several uncertain microstructural parameters to assess their influence on the modelled velocity and attenuation response. This sensitivity analysis showed that permeability and gas bubble radius had the strongest effects on the modelled P-wave velocity and attenuation over the frequency range considered, and that variations in these two parameters provided the closest match to the laboratory data. We therefore focus on these two parameters in Figures 10 and 11. The permeability and gas bubble-radius values shown in the figure legends should be interpreted as plausible sensitivity ranges used to explore model behaviour, rather than direct measurements of the ice cores. In these tests, total porosity and fluid saturation were kept fixed for each core;

https://doi.org/10.5194/egusphere-2026-4816
Preprint. Discussion started: 5 November 2026
© Author(s) 2026. CC BY 4.0 License.

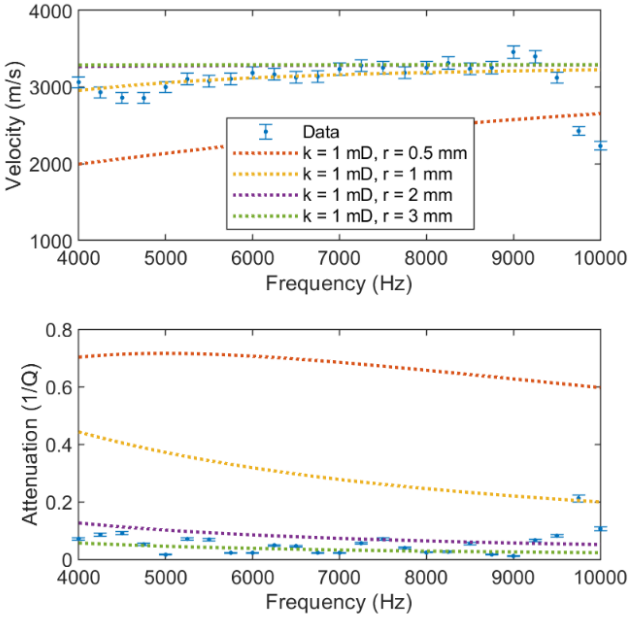
changing bubble radius changed only the characteristic inclusion size used in the gas-bubble response, not the total pore volume.

Model results demonstrate that P-wave velocity and attenuation are particularly sensitive to gas bubble radius and permeability at frequencies below 10 kHz. Increasing bubble radius reduces the modelled attenuation and increases the modelled velocity in both frequency ranges (Figure 10a and 11a). By contrast, increasing permeability increases the modelled attenuation and decreases the velocity in both frequency ranges (Figure 10b and 11b), although this decrease in velocity is more prominent in lower frequency range. This opposite trend between changes in permeability and gas bubble radius shows there can be a unique range when both these properties can result in similar velocity and attenuation values. The bubble radius adopted in the modelling represents a physically plausible millimetre scale inclusion size consistent with microscopic observations of glacier ice, where typical bubble diameters are submillimetre to millimetre scale and larger millimetre scale air–water cavities can occur locally in shallow ice near the firn–ice transition, prior to compression with depth (Bader, 1950; Gow, 1969; Li et al., 2023).

Importantly, similar velocity spectra can be produced by distinct combinations of permeability and bubble radius, indicating strong parameter trade-offs. At higher frequencies, modelled velocities converge toward a common asymptotic value, reflecting dominance of the elastic frame response. Velocity measurements alone are therefore insufficient to uniquely constrain microstructural properties. Attenuation magnitude and frequency dependence provide additional discriminatory power but do not fully eliminate non-uniqueness.

https://doi.org/10.5194/egusphere-2026-4816
Preprint. Discussion started: 5 November 2026
© Author(s) 2026. CC BY 4.0 License.

a) Effect of Gas Bubble Radius



b) Effect of Permeability

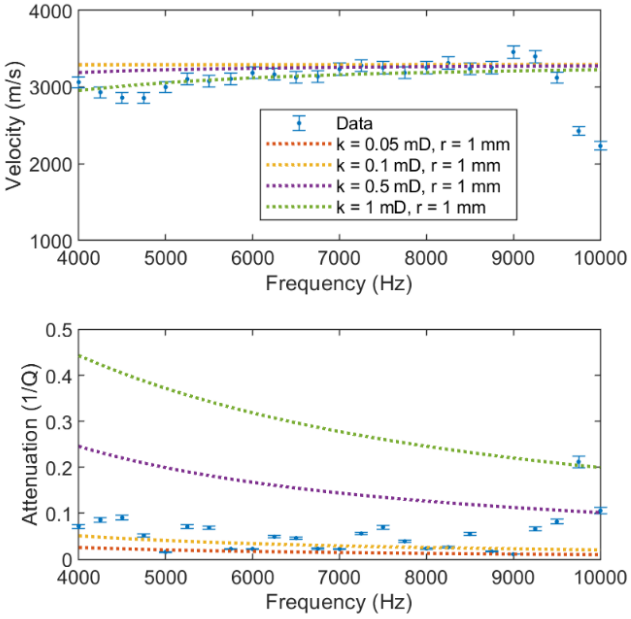
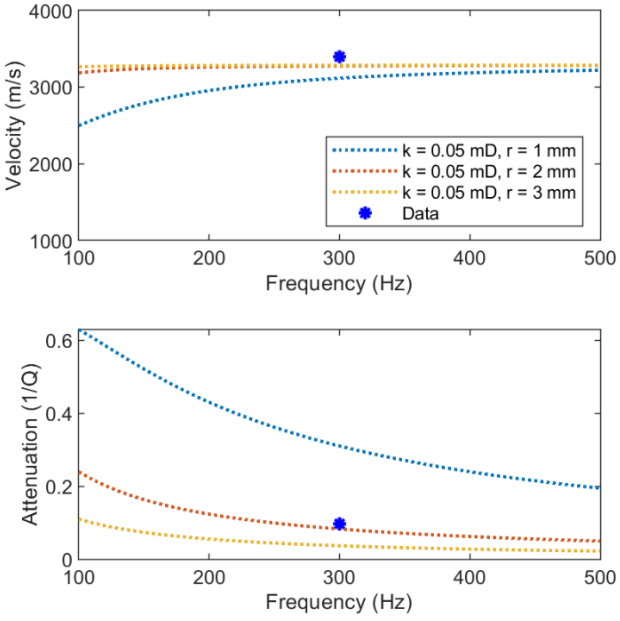


Figure 10: Comparison of effective medium modelling with pulse tube measurements for varying a) the gas bubble radius and b) permeability. Gas bubble radius is shown in the legend as r with units of millimetre; permeability is given as 'k' in units of millidarcy.

507

https://doi.org/10.5194/egusphere-2026-4816
Preprint. Discussion started: 5 November 2026
© Author(s) 2026. CC BY 4.0 License.

a) Effect of Gas Bubble Radius



b) Effect of Permeability

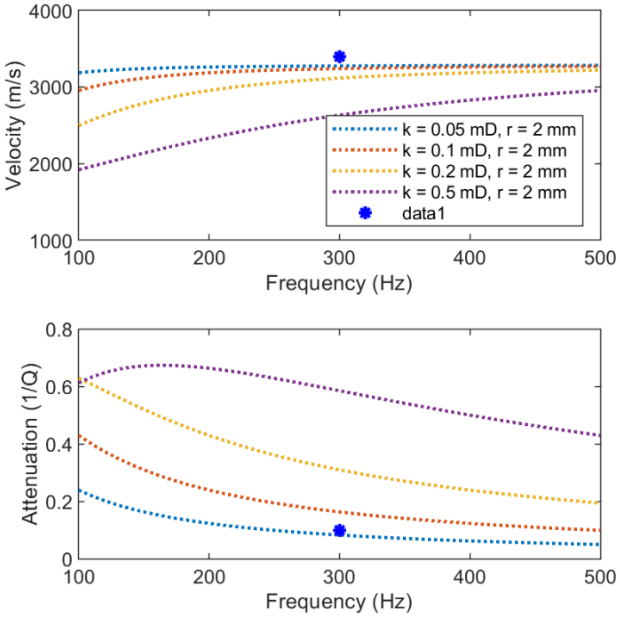


Figure 11: Comparison of effective medium modelling with resonant column measurements on ice core4 (blue star), for varying a) the gas bubble radius (r) and b) permeability (k). Gas bubble radius is shown in legend with units of millimetres, and permeability in millidarcy.

508

https://doi.org/10.5194/egusphere-2026-4816
Preprint. Discussion started: 5 November 2026
© Author(s) 2026. CC BY 4.0 License.

4. Implications and limitations for seismic and through-ice acoustic measurements

Despite the inherent non-uniqueness highlighted above, the modelling identifies physically plausible mechanisms capable of explaining the observed reduction in velocity and increase in attenuation in samples with higher inclusion content. The consistency of sensitivity trends across both frequency bands suggests that similar dissipation processes operate over a wide frequency range.

The laboratory results are directly relevant to measurements in which part or all the observed wavefield propagates within the ice. These include seismic reflection and refraction surveys, guided-wave and distributed acoustic sensing measurements, cross-hole observations, and through-ice acoustic methods that identify reflections from both the ice–water and ice–air interfaces. Such methods are used by researchers investigating the thickness, mechanical properties, and internal structure of sea ice, lake ice, and glacier ice. In these configurations, the assumed P- or S-wave velocity affects the conversion of measured travel times or dispersion characteristics into ice thickness. Seismic and distributed acoustic sensing studies have shown that reflected phases and guided-wave dispersion can provide constraints on ice thickness when the elastic properties of the ice are appropriately considered

For a simplified normal-incidence measurement involving two-way propagation through the ice, thickness can be expressed as

$$h = \frac{V_p \Delta t}{2}, \tag{8}$$

where h is ice thickness, $V_p$is the P-wave velocity in the ice, and $\Delta t$is the two-way travel time through the ice. If travel-time uncertainty is small, the first-order fractional error in thickness is approximately equal to the fractional error in the assumed velocity:

$$\frac{\Delta h}{h} \approx \frac{\Delta V_p}{V_p}. \tag{9}$$

At frequencies below ~10 kHz modelled velocity variations associated solely with inclusion properties can exceed 20%. This is consistent with the approximately 20–25% difference between the end-member P-wave velocities measured using the acoustic pulse tube. If unaccounted for, such variations would translate directly into comparable bias in ice thickness estimates derived from travel time measurements. For example, for a 1 m thick ice layer, interpreting the same travel time using the measured end-member acoustic velocities would produce apparent thicknesses of approximately 0.80–1.25 m, corresponding to potential errors of approximately 0.20–0.25 m. These values illustrate the sensitivity of the thickness estimate to the selected velocity rather than the accuracy of a particular field instrument or retrieval method.

The implications for conventional upward-looking sonar are different. These systems normally measure the travel time through seawater to the ice–water interface and therefore primarily determine ice draft, with total thickness subsequently estimated using hydrostatic assumptions and estimates of ice and snow density (Hudson, 1990; Melling and Riedel, 1995; Wadhams, 1987). The elastic-wave velocity within the ice does not directly control this water-column range measurement. However, inclusion-related changes in bulk ice density may affect the hydrostatic conversion from draft to total thickness. Changes in acoustic impedance, attenuation, and scattering may also affect the amplitude and spectral characteristics of the reflection from the ice–water interface.

More direct application of the present results arises in broadband acoustic methods that resolve reflections from both the ice–water and ice–air interfaces. In these measurements, the time separation between the two returns depends on propagation through the ice and therefore on the assumed ice velocity. Bassett et al. (2015, 2020) demonstrated the potential of broadband acoustic backscatter for characterising sea ice and directly estimating first-year sea-ice thickness under favourable conditions. Numerical and field studies also show that interpretation of these measurements depends on coupled effects from thickness, elastic properties, attenuation, and interface

https://doi.org/10.5194/egusphere-2026-4816
Preprint. Discussion started: 5 November 2026
© Author(s) 2026. CC BY 4.0 License.

roughness (Chotiros et al., 2023). The velocity and attenuation ranges measured here provide laboratory constraints for assessing these effects, particularly at frequencies lower than those used in most previous broadband echo-sounding studies.

Broadband measurements that constrain both velocity and attenuation may provide additional information on inclusion-related heterogeneity when combined with independent observations or prior information. Independent measurements from ice coring, ground-penetrating radar, electromagnetic methods, or collocated seismic surveys could provide local constraints on ice thickness. If an independent thickness measurement is combined with a measured two-way travel time through the ice, an effective P-wave velocity can be estimated as

$$V_{p,\mathrm{eff}} = \frac{2h_{\mathrm{ind}}}{\Delta t}, \tag{10}$$

where h_{ind} is the independently measured thickness. Repeated measurements from an autonomous underwater vehicle or another mobile acoustic platform could then potentially map spatial variations in effective ice velocity, attenuation, or acoustic impedance.

Such variations may provide information about relative changes in inclusion-related heterogeneity. However, they should not be interpreted as a unique measurement of inclusion concentration. The modelling demonstrates that distinct combinations of porosity, permeability, gas-bubble radius, and unfrozen-water saturation can produce similar velocity and attenuation responses. Combining travel time with attenuation, frequency dependence, temperature, salinity, and independent observations may reduce this ambiguity, but would not necessarily eliminate it.

We stress that the present modelling is intended as a first-order interpretation rather than a formal inversion. Future work incorporating direct measurements of permeability, bubble-size distributions, inclusion geometry, and unfrozen-water content would enable more quantitative parameter estimation and an improved assessment of model uniqueness.

The laboratory ice cores used in this study were formed from freshwater and therefore do not contain the saline brine inclusions characteristic of natural sea ice. In sea ice, salt rejection during freezing produces brine pockets and brine-channel networks that introduce additional attenuation and scattering mechanisms, with strong temperature and frequency dependence (Garrison, Knapp, et al., 1991; Wadhams, 1987). These effects influence the detectability of reflections from the ice–air interface in sonar-based thickness measurements, particularly at higher acoustic frequencies (Bassett et al., 2015, 2020).

The structure and connectivity of fluid inclusions in natural sea ice also evolve with ice age and environmental conditions. Temperature, salinity, growth rate, brine drainage, deformation, and melt–refreeze processes can modify the volume, geometry, and connectivity of inclusions. Freshwater laboratory ice instead contains air bubbles and possible unfrozen water as its dominant inclusion phases and is therefore more closely analogous, in a microstructural sense, to glacial ice.

Acoustic and seismic studies of glaciers demonstrate that air inclusions alone can produce substantial changes in wave velocity and attenuation, even in the absence of saline brine, and that these effects influence the travel times and reflection strengths used to infer ice thickness (Podolskiy and Walter, 2016). This is particularly relevant to lower-frequency acoustic and seismic measurements, for which reduced attenuation may improve penetration and the detectability of interfaces (Booth et al., 2020; Nziengui-Bâ et al., 2023).

The laboratory experiments presented here therefore provide a controlled framework for isolating the influence of porosity, permeability, and inclusion size on elastic-wave propagation. The resulting velocity and attenuation ranges provide baseline constraints relevant to glacial ice and to the solid ice framework of sea ice, while salinity-related brine effects represent an additional source of velocity variation, scattering, and attenuation in natural sea ice (Bassett et al., 2020; Chotiros et al., 2023).

https://doi.org/10.5194/egusphere-2026-4816
Preprint. Discussion started: 5 November 2026
© Author(s) 2026. CC BY 4.0 License.

5. Conclusions

We have presented novel laboratory data for four synthetic ice cores, including broadband (4–10 kHz) P-wave velocity and attenuation measurements and low-frequency (~300 Hz) P- and S-wave velocity and attenuation measurements obtained using acoustic pulse tube and resonant column methods respectively. We developed a method for forming synthetic ice cores that imitates key aspects of natural sea ice formation, namely freezing from above under cooled air with circulation of water below. This approach enabled the production of cylindrical synthetic ice cores with contrasting bulk density and fluid inclusion content.

Pulse tube measurements at 4–10 kHz indicate that the lower-density core (851.8 kg m^{-3}) has a lower mean P-wave velocity of 2465 ± 146 m s^{-1} than the higher-density core (903 kg m^{-3}), which had a mean P-wave velocity 3090 ± 273 m s^{-1}. The resonant column results show broadly similar trends at ~300 Hz. The lower-density core (886 kg m^{-3}) showed a P-wave velocity of 3100 ± 120 m s^{-1}, whereas the higher-density core (905 kg m^{-3}) showed a P-wave velocity of 3400 ± 180 m s^{-1}. The lower-density core also showed a lower shear wave velocity (1050–1150 m s^{-1}) than the higher-density core, which had an S-wave velocity of approximately 1250 m s^{-1}. This velocity difference indicates that increased inclusion content substantially reduces the effective elastic stiffness of the ice. The lower-density core also showed strain-dependent S-wave velocity and attenuation, suggesting that inclusion-related microstructure plays an important role in controlling shear stiffness and damping.

Bulk density was measured directly for each core and provides the primary basis for comparison in this study. Density-derived porosity estimates of 1.45–7.1% were calculated by assuming a pure-ice density of 917 kg m^{-3}; these values should be interpreted as upper-bound estimates of air-inclusion volume, because the contribution of unfrozen water to the density deficit was not independently constrained.

We adapted a Biot-based effective medium wave propagation model to porous ice containing air and unfrozen water to investigate mechanisms controlling frequency-dependent P-wave velocity and attenuation. The modelling shows that gas bubble size and permeability both exert strong control on the predicted elastic-wave response, and that trade-offs between these parameters can produce similar velocity and attenuation values. The modelling therefore provides a first-order physical framework for interpreting the laboratory observations, rather than a unique inversion for microstructural properties.

Overall, this study provides a new laboratory dataset across two frequency range, on elastic-wave propagation in synthetic ice formed under controlled conditions relevant to sea ice analogues. The results show that air inclusions and possible unfrozen water can produce P-wave velocity variations of approximately 20–25%, which, if unaccounted for, may introduce substantial errors in sea ice thickness estimates derived from through-ice acoustic or seismic travel times. Although the cores were formed from freshwater and therefore do not reproduce the full brine microstructure of natural saline sea ice, they provide a useful baseline for isolating the effects of inclusions on elastic-wave velocity and attenuation. These findings help to constrain the range of acoustic and seismic properties that should be considered in the interpretation of field measurements of sea ice thickness and mechanical behaviour.

Acknowledgements:

The laboratory measurements were funded through the Defence and Security Accelerator (DASA), and the modelling work was subsequently supported by NOC internal RISC funding through the INPER project. We have used National Oceanography Centre approved Microsoft Co-pilot for grammar checks.

https://doi.org/10.5194/egusphere-2026-4816
Preprint. Discussion started: 5 November 2026
© Author(s) 2026. CC BY 4.0 License.

Appendix A

This section describes how the reflection impulse response of an ice sample is isolated from the response of the pulse tube. The impulse response of the ice sample is obscured by multiple reflections from the high reflectivity pulse tube terminations (end caps) and impedance discontinuities from hydrophone ports in the wall of the tube, etc. It is, therefore, necessary to remove these multiple reflections to obtain an accurate sample impulse response.

A schematic diagram of the pulse tube and accompanying signal flow diagram is shown in Figure A1. The following model assumes a 1D (pressure only varies along the length of the tube) linear, causal acoustic system. This 1D model of the pulse tube is developed in the frequency domain, that is, all the variables and transfer functions, discussed below are functions of frequency. In the de-embedding procedure, we perform operations on discrete frequency domain data transformed, via FFT, from discrete (sampled) time-domain data. Thus, the equations given below are evaluated at each discrete frequency determined by the time domain sampling frequency and length of the time domain series. This evaluation results in the frequency dependant reflection response of the sample which may then be transformed to the time domain via an inverse FFT for a more intuitive representation of the impulse response of the sample.

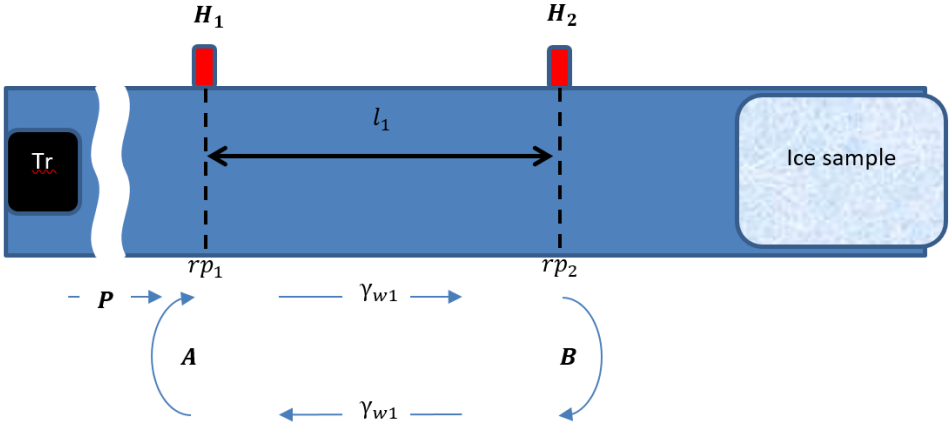


Figure A1: Schematic diagram and accompanying signal flow diagram of the pulse tube. Symbols define parameters used in the equations in the main text.

The acoustic source transducer, labelled Tr, is shown to the left of the tube. The transducer produces an incident pressure wave P. The sampling hydrophones are shown in red. The complex transfer functions (the relationship between pressure and recorded voltage) of the hydrophones are denoted by H_1 and H_2. Two notional reference planes, rp_1 and rp_2, coincident with the centres of the hydrophones, are shown by black dashed lines. The complex reflection responses of the parts of the pulse tube external to the region between the reference planes are labelled A and B. These reflection responses are infinite series that include all partial and multiple reflections. A known distance, l_1, separates the two hydrophones. The complex propagation coefficient, γ_{w1}, of the water filled tube in the region between the hydrophones, including absorption, is given by

$$\gamma_{w1} = e^{-i\omega\frac{l_1}{v_w}}, \tag{A-1}$$

where ω is angular frequency, l_1 is the distance between hydrophones, and v_w is the complex velocity of sound in water (including absorption losses).

Using a scattering matrix based approach, it can be shown that the complex ratio of the transformed measured output of hydrophone 1 and 2 at each frequency is given by the ratio, R;

$$R = \left(\frac{H_1}{H_2}\right)\frac{1+\gamma_{w1}^2 B}{\gamma_{w1}+\gamma_{w1}B}. \tag{A-2}$$

https://doi.org/10.5194/egusphere-2026-4816
Preprint. Discussion started: 5 November 2026
© Author(s) 2026. CC BY 4.0 License.

It can be seen that ratio R is only a function of the ratio of hydrophone transfer functions, the propagation coefficient of the water between the hydrophones and reflection response B. The complex transfer function of the source transducer and the reflection response A are eliminated by taking this ratio.

The ratio of hydrophone transfer functions, H_1/H_2, can be obtained through calibration and γ_{w1} can be estimated with a high degree of precision from well established models of water sound speed. Thus, the reflection response B may be obtained by rearranging eqn. A-2, yielding;

$$B = \left(\frac{1}{\gamma_{w1}}\right)\frac{R\gamma_{w1}-\left(\frac{H_1}{H_2}\right)}{\left(\frac{H_1}{H_2}\right)\gamma_{w1}-R}. \quad \text{(A-3)}$$

The reflection response B contains the reflection response of the sample and any reflections from within the region between rp_2 and the sample.

https://doi.org/10.5194/egusphere-2026-4816
Preprint. Discussion started: 5 November 2026
© Author(s) 2026. CC BY 4.0 License.

References:

Agnew, R. S., Pearce, E., Karplus, M., Ranganathan, M., Hoffman, A. O., Hunt, M., … Young, T. J. (2026). Active and passive seismic surveys over the grounding zone of Eastwind Glacier, Antarctica. *Seismological Research Letters*, *97*, 591–605. https://doi.org/10.1785/0220250024

Ainslie, M. A., & McColm, J. G. (1998). A simplified formula for viscous and chemical absorption in sea water. *Journal of the Acoustical Society of America*, *103*(3), 1671–1672. https://doi.org/10.1121/1.421258

Bader, H. (1950). The Significance of Air Bubbles in Glacier Ice. *Journal of Glaciology*, *1*(8), 443–451. https://doi.org/10.3189/S002214300001279X

Bassett, C., Lavery, A. C., Wilkinson, J. P., Maksym, T., & Courville, Z. R. (2018). Inferring first-year sea ice thickness using broadband echosounders. *The Journal of the Acoustical Society of America*, *144*(3_Supplement), 1819–1819. https://doi.org/10.1121/1.5068024

Bassett, C., Lavery, A. C., Lyons, A. P., Wilkinson, J. P., & Maksym, T. (2020). Direct inference of first-year sea ice thickness using broadband acoustic backscattering. *The Journal of the Acoustical Society of America*, *147*(2), 824–838. https://doi.org/10.1121/10.0000619

Bassett, C., Lavery, A. C., Maksym, T., & Wilkinson, J. P. (2015). Laboratory measurements of high-frequency, acoustic broadband backscattering from sea ice and crude oil. *The Journal of the Acoustical Society of America*, *137*(1), EL32–EL38. https://doi.org/10.1121/1.4902421

Bassett, C., Lavery, A. C., Maksym, T., & Wilkinson, J. P. (2016). Broadband acoustic backscatter from crude oil under laboratory-grown sea ice. *The Journal of the Acoustical Society of America*, *140*(4), 2274–2287. https://doi.org/10.1121/1.4963876

Biot, M. A. (1956a). Theory of Propagation of Elastic Waves in a Fluid-Saturated Porous Solid. I. Low-Frequency Range. *The Journal of the Acoustical Society of America*, *28*(2), 168–178. https://doi.org/10.1121/1.1908239

Biot, M. A. (1956b). Theory of Propagation of Elastic Waves in a Fluid-Saturated Porous Solid. II. Higher Frequency Range. *The Journal of the Acoustical Society of America*, *28*(2), 179–191. https://doi.org/10.1121/1.1908241

Bocquet, M., Fleury, S., Rémy, F., & Piras, F. (2024). Arctic and Antarctic Sea Ice Thickness and Volume Changes From Observations Between 1994 and 2023. *Journal of Geophysical Research: Oceans*, *129*(11), e2023JC020848. https://doi.org/https://doi.org/10.1029/2023JC020848

Booth, A. D., Christoffersen, P., Schoonman, C., Clarke, A., Hubbard, B., Law, R., … Chalari, A. (2020). Distributed Acoustic Sensing of Seismic Properties in a Borehole Drilled on a Fast-Flowing Greenlandic Outlet Glacier. *Geophysical Research Letters*, *47*(13), e2020GL088148. https://doi.org/10.1029/2020GL088148

Chotiros, N. P., Bayrakci, G., Sanford, O., Clarke, T., & Best, A. I. (2023). Simulation of acoustic reflection and backscatter from arctic sea-ice. *The Journal of the Acoustical Society of America*, *153*(6), 3258. https://doi.org/10.1121/10.0019636

Clayton, C. R. I., Priest, J. A., & Best, A. I. (2005). The effects of disseminated methane hydrate on the dynamic stiffness and damping of a sand. *Géotechnique*, *55*(6), 423–434. https://doi.org/10.1680/geot.2005.55.6.423

Garrison, G. R., Knapp, J. S., & Tatro, C. A. (1991). Acoustic properties of Arctic sea ice. *Journal of the Acoustical Society of America*, *89*, 2265–2276. https://doi.org/10.1121/1.400850

Garrison, G. R., Francois, R. E., & Wen, T. (1991). Acoustic reflections from arctic ice at 15-300 kHz. *Journal of the Acoustical Society of America*, *90*(2), 973–984. https://doi.org/10.1121/1.401965

Hills, D., Lawless, B., Khangerey, R., Wilkinson, J., & Marsh, L. A. (2025). Towards the Measurement of Sea-Ice Thickness Using a Time-Domain Inductive Measurement System. *Sensors*, *25*(2), 1–20. https://doi.org/10.3390/s25020510

Hobbs, P. V. (2010). *Ice Physics*. Oxford University Press. https://doi.org/10.1093/acprof:oso/9780199587711.001.0001

Hudson, R. (1990). Annual measurement of sea-ice thickness using an upward-looking sonar. *Nature*, *344*(6262), 135–137. https://doi.org/10.1038/344135a0

Johnson, S., Randall, D. G., Rampai, T., Vichi, M., & Skatulla, S. (2021). Growing Artificial Sea Ice and The Importance of Seeding.

https://doi.org/10.5194/egusphere-2026-4816
Preprint. Discussion started: 5 November 2026
© Author(s) 2026. CC BY 4.0 License.

Langleben, M. P. (1969). Attenuation of sound in sea ice, 10–500 kHz. *Journal of Glaciology*, *8*(54), 399–406. https://doi.org/10.3189/S0022143000026988

Leclaire, P., Cohen-Ténoudji, F., & Aguirre-Puente, J. (1994). Extension of Biot's theory of wave propagation to frozen porous media. *The Journal of the Acoustical Society of America*, *96*(6), 3753–3768. https://doi.org/10.1121/1.411336

Light, B., Maykut, G. A., & Grenfell, T. C. (2003). Effects of temperature on the microstructure of first-year Arctic sea ice. *Journal of Geophysical Research: Oceans*, *108*(2), 1–16. https://doi.org/10.1029/2001jc000887

Mavko, G., Mukerji, T., & Dvorkin, J. (2009). *The Rock Physics Handbook*. Cambridge: Cambridge University Press. https://doi.org/10.1017/CBO9780511626753

McCann, C., Sothcott, J., & Best, A. I. (2014). A new laboratory technique for determining the compressional wave properties of marine sediments at sonic frequencies and in situ pressures. *Geophysical Prospecting*, *62*(1), 97–116. https://doi.org/10.1111/1365-2478.12079

Melling, H., & Riedel, D. A. (1995). The underside topography of sea ice over the continental shelf of the Beaufort Sea in the winter of 1990. *Journal of Geophysical Research*, *100*, 13641–13653. https://doi.org/10.1029/95JC00309

Meyer, A., Eliseev, D., Heinen, D., Linder, P., Scholz, F., Weinstock, L. S., … Zierke, S. (2019). Attenuation of sound in glacier ice from 2 to 35 kHz, 1381–1394.

North, L. J., & Best, A. I. (2019). *Technical Report: The Acoustic Properties of Sea Ice – a preliminary study*. R&C report 85, National Oceanography Centre, Southampton, UK.

Nziengui-Bâ, D., Coutant, O., Moreau, L., & Boué, P. (2023). Measuring the thickness and Young's modulus of the ice pack with DAS, a test case on a frozen mountain lake. *Geophysical Journal International*, *233*(2), 1166–1177. https://doi.org/10.1093/gji/ggac504

Podolskiy, E. A., & Walter, F. (2016). Cryoseismology. *Reviews of Geophysics*, *54*, 708–758. https://doi.org/10.1002/2016RG000526

Priest, J. A., Best, A. I., & Clayton, C. R. I. (2005). A laboratory investigation into the seismic velocities of methane gas hydrate-bearing sand. *Journal of Geophysical Research*, *110*(B4), B04102. https://doi.org/10.1029/2004JB003259

Rajan, S. D., Frisk, G. V, Doutt, J. A., Sellers, C. J., Rajan, D., Frisk, G. V, … Sellers, J. (2017). Determination of compressional wave and shear wave speed profiles in sea ice by crosshole tomography—Theory and experiment, *721*(1993). https://doi.org/10.1121/1.405436

Sammonds, P. R., Montagnat, M., Bons, P. D., & Schneebeli, M. (2017). Ice Microstructures and Microdynamics. *Philosophical Transactions of the Royal Society A*, *375*, 20160438. https://doi.org/10.1098/rsta.2016.0438

Senetakis, K., Madhusudhan, B. N., & Anastasiadis, A. (2016). Wave propagation attenuation and threshold strains of fully saturated soils with intraparticle voids. *Journal of Materials in Civil Engineering*, *28*(2), 1–11.

Sumata, H., de Steur, L., Divine, D. V, Granskog, M. A., & Gerland, S. (2023). Regime shift in Arctic Ocean sea ice thickness. *Nature*, *615*(7952), 443–449. https://doi.org/10.1038/s41586-022-05686-x

Sun, B., Wen, J., He, M., Kang, J., Luo, Y., & Yuansheng, L. (2003). Sea ice thickness measurement and its underside morphology analysis using radar penetration in the Arctic Ocean. *Science in China Series D: Earth Sciences*, *46*(11), 1151–1160. https://doi.org/10.1360/02yd0033

Sutiyoso, H. S., Sahoo, S. K., North, L. J., Minshull, T. A., Falcon-Suarez, I. H., & Best, A. I. (2024). Laboratory measurements of water saturation effects on the acoustic velocity and attenuation of sand packs in the 1–20 kHz frequency range. *Geophysical Prospecting*, *72*(9), 3316–3337. https://doi.org/https://doi.org/10.1111/1365-2478.13607

Sutiyoso, H. S., Sahoo, S. K., North, L. J., Falcon-Suarez, I. H., Minshull, T. A., & Best, A. I. (2025). Laboratory Measurement of Sonic (1–20 kHz) P-Wave Velocity and Attenuation During Melting of Ice-Bearing Sand. *Journal of Geophysical Research: Solid Earth*, *130*(4). https://doi.org/10.1029/2024JB030465

Sutiyoso, H. S., Sahoo, S. K., Falcon-suarez, I. H., North, L. J., Minshull, A., & Best, A. I. (2026). Pressure effects on acoustic (1 – 20 kHz) velocity and attenuation during the melting of ice-bearing sand, *91*(3), 1–14.

Tollefsen, D., van Walree, P., Jenserud, T., & Forsmo, V. (2023). Under-ice mid-frequency acoustic

https://doi.org/10.5194/egusphere-2026-4816
Preprint. Discussion started: 5 November 2026
© Author(s) 2026. CC BY 4.0 License.

transmission and communication in two Arctic Ocean environments. *JASA Express Letters*, *3*, 026004. https://doi.org/10.1121/10.0017325

Vogt, C., Laihem, K., & Wiebusch, C. (2008). Speed of sound in bubble-free ice. *The Journal of the Acoustical Society of America*, *124*(6), 3613–3618. https://doi.org/10.1121/1.2996304

Wadhams, P. (1987). Sea ice thickness measurements from acoustic methods. *Cold Regions Science and Technology*, *13*, 169–179. https://doi.org/10.1016/0165-232X(87)90007-3

Walter, F., Gräff, D., Lindner, F., Paitz, P., Köpfli, M., Chmiel, M., & Fichtner, A. (2020). Distributed acoustic sensing of microseismic sources and wave propagation in glaciated terrain. *Nature Communications*, *11*, 2436. https://doi.org/10.1038/s41467-020-15824-6

Weissenberger, J., & Grossmann, S. (1998). Experimental formation of sea ice: Importance of water circulation and wave action for incorporation of phytoplankton and bacteria. *Polar Biology*, *20*(3), 178–188. https://doi.org/10.1007/s003000050294

Xu, H., Xing, J., Zuo, G., & Wei, J. (2025). Cross-hole acoustic tomography of Arctic sea ice: Insights into temperature-driven velocity and attenuation variations. *Intelligent Marine Technology and Systems*. https://doi.org/10.1007/s44295-025-00078-z